A-POSTERIORI ERROR ESTIMATION FOR THE FINITE POINT METHOD WITH APPLICATIONS TO COMPRESSIBLE FLOW

Enrique Ortega[1], Roberto Flores[1], Eugenio Oñate[1] and Sergio Idelsohn[1,2]

[1] Centre Internacional de Mètodes Numèrics en Enginyeria (CIMNE)
Technical University of Catalonia (UPC)
08034 Barcelona, Spain

[2] Institució Catalana de Recerca i Estudis Avançats (ICREA)

Abstract. An *a-posteriori* error estimate with application to inviscid compressible flow problems is presented. The estimate is a surrogate measure of the discretization error, obtained from an approximation to the truncation terms of the governing equations. This approximation is calculated from the discrete nodal differential residuals using a reconstructed solution field on a modified stencil of points. Both the error estimation methodology and the flow solution scheme are implemented using the Finite Point Method, a meshless technique enabling higher-order approximations and reconstruction procedures on general unstructured discretizations. The performance of the proposed error indicator is studied and applications to adaptive grid refinement are presented.

1 INTRODUCTION

Numerical simulation plays an increasingly important role in most fields of science and engineering. Thus arises the need for better identification and quantification of numerical errors, not only as a means to improve the numerical solutions (e.g. through grid adaptation) but also to determine the accuracy and reliability of the computational code and the results. Error analyses developed in the framework of verification and validation (V&V) are becoming standard practices in numerical simulation, see [1-4] for an overview.

Among the different errors affecting numerical accuracy, the most relevant are discretization, iterative convergence and round-off errors. While iterative convergence and round-off errors can be estimated and controlled to a good extent, the discretization error, which tends to dominate, is more difficult to evaluate. Therefore, determining the accuracy of a numerical simulation relies mainly on the identification and quantification of discretization errors. Numerous techniques, mostly based on *a-posteriori* estimators, have been developed with this aim. The most typical approaches are briefly reviewed below to establish the theoretical framework of the problem.

One of the first effective techniques for error estimation in a single grid was proposed by Zienkiewicz and Zhu (ZZ) in the context of the Finite Element Method (FEM) [5]. In this approach a higher accuracy estimate of the solution gradients is reconstructed from the super-convergent points of the discretization (valid for smooth solution fields, with some exceptions depending on mesh topology). This high-order estimate is compared against the "ordinary" approximate gradients computed directly from the nodal values. The difference between the two gradient fields is used as error estimator, converging to the true error as the grid is refined [6]. The main advantage of the ZZ estimator is that it provides reasonable measures of local and global errors at a low computational cost. In solid mechanics and heat transfer, this estimator can give true stress and heat-flux errors, respectively, allowing goal-oriented error estimation. However, a direct relation with variables or functionals of interests (e.g. lift or drag) has not been found in flow problems. Thus, applications of the ZZ estimator in fluid mechanics have been mostly restricted to grid adaptation.

Other popular *a-posteriori* error estimators, also conceived within the FEM framework, are based on differential residuals of the discrete solution [7, 8]. Though typically these residuals are obtained by inserting an approximate solution into a modified form of the governing equations, tey can be also computed by using an enhanced solution field with the same set of discrete equations. Non-zero local (and global) residual values can be related to an imbalance in the governing equations and this, in turn, to errors in the conserved quantities affecting the problem solution and derived output functionals (although the relationships are not straightforward). In this sense, some applications using residual imbalances (e.g. in kinetic energy, momentum, etc.) have proven useful in guiding automatic grid adaptation and also as surrogate indicators for errors in derived output quantities; see for instance [9, 10] and more recently [11], where power forms of mass and momentum residuals are used to guide mesh adaptivity in incompressible flow problems.

An extension of residual methods which provides goal-oriented error estimates is based on the solution of adjoint-problems [12]. Although these methods have a higher complexity and require the solution of a dual problem, promising applications can be found in the literature, see for example [13] and [14]. The latter work evaluates the influence of artificial dissipation on the discretization error and the computed aerodynamic forces.

Another class of error estimation methods directly models (and solves) the generation and transport of error by means of the so-called Discrete Error Transport equations (DET) [15-17]. These are generally obtained from the truncation terms of the governing equation, i.e. the

difference between the original equation and its discrete counterpart. Since explicit forms of the truncation terms are difficult to obtain in general problems, approximate expressions have to be derived; these usually have a close connection with differential residuals [18]. The key role played by truncation terms in DET equations makes them suitable candidates to measure discretization errors. An application in which a normalized form of the truncation error is adopted as an approximate solution of DET equations is given in [19]. Moreover, the proportionality between the local truncation terms and the discretization error is demonstrated in [20] over a considerable range of problems and simple discretization schemes. This kind of estimators is also efficient driving mesh adaptation because the truncation terms account for mesh quality and flow features contributions to the discretization error; see applications in [18, 21-23]. Other methods closely related to truncation error and differential residuals are those based on multi-grid operators [24, 25].

An important family of methods, commonly adopted in V&V due to their reliability, uses extrapolation to estimate solution errors. The most popular technique is based on Richardson extrapolation [26, 27] and requires two grids (or three if the order of accuracy of the scheme is not known) to compute a higher-order estimate of the numerical solution which is used to evaluate the error. This methodology, also known as *h*-extrapolation, has proved a reliable error estimator for any quantity of interest (pointwise values as well as solution functionals, see [28, 29]), and is independent of the underlying problem discretization. However, *h*-extrapolation has the disadvantage of requiring solutions on different grids subject to certain conditions which are sometimes difficult to achieve (e.g. integer refinement ratios and solutions in the asymptotic range of convergence [3, 30, 31]). Among the estimators based on Richardson's extrapolation it is worth mentioning Roache's Grid Convergence Index (GCI) [32], which provides conservative confidence intervals (uncertainty) for the extrapolated error estimates. In addition, non-integer refinement ratios can be employed with the GCI, simplifying the generation of the computational models.

Also based on extrapolation, there are single-grid techniques where the higher-order solution estimates are obtained by increasing the order of accuracy of the underlying numerical scheme (p-extrapolation). While these techniques can be implemented in a relatively simple manner in structured grids, they cannot be easily extended to unstructured grids and general discretization methods. Applications of p-extrapolation can be found in [33-35].

In the context of meshless methods, the error estimation methodologies follow the general lines mentioned above, but aim at exploiting the advantages of these methods regarding

topological requirements and data structures. For example, meshless approaches have a considerable potential to deal with general unstructured discretizations and high-order approximations, simplifying the implementation of error estimation procedures. Among the first meshless applications, error estimates based on residuals [36] and wavelets [37] can be found. More recently, enhanced, recovered, or higher-order solution fields have been employed to obtain error estimates and indicators [38-42]. Error functionals derived from the construction of the approximation have also been proposed, see for instance [43-45] and [46], where the error estimate is used as an *a-priori* indicator to optimize the approximation subdomains. The applications of these methods have mostly focused on local improvement of the solution (reducing discretization errors) through *p* or *h*-adaptation. A recent application to goal-oriented error estimation can be found in [47].

In this work an *a-posteriori* meshless estimate of the discretization error is proposed. The estimate is based on an approximate form of the truncation terms of the governing equations which is obtained through nodal discrete differential residuals. Following typical approaches in residual-based error estimation, the residuals are evaluated using a reconstructed solution field on a modified stencil of points. The proposed methodology is developed in the context of the Finite Point Method (FPM) [48-50], but it could be also extended to conventional mesh-based discretization techniques with minor modifications.

This article is organized as follows. The FPM discretization technique and the flow solver used are described in Sections 2 and 3, respectively. The proposed error estimate is presented in Section 4, together with tests showing the reliability of the procedure. Applications of the technique to adaptive flow problems are provided in Section 5. Finally, the most relevant conclusions of this work and future lines of research are outlined in Section 6.

2 THE FPM APPROXIMATION

This section describes the main aspects of the FPM approximation. Assume that $\phi(\mathbf{x})$ is an unknown function defined in a domain Ω which is discretized by a set of n points $\boldsymbol{x}_i$. Let Ω be covered by subsets of np points Ω_i (clouds of points) consisting of a point $\boldsymbol{x}_i$ called *star point* and a collection of surrounding points $\boldsymbol{x}_j$ as shown in Figure 1. Then, an approximation of $\phi(\mathbf{x})$ in Ω_i can be obtained by

$$\phi(\boldsymbol{x}) \approx \hat{\phi}(\boldsymbol{x}) = \mathbf{p}^{\mathrm{T}}(\boldsymbol{x})\,\boldsymbol{\alpha} \tag{1}$$

where **p** is a vector of size *m* containing monomial basis functions and $\boldsymbol{\alpha}$ is a vector of unknown coefficients. In this work complete quadratic polynomial bases are employed (e.g. $\mathbf{p}^{\mathrm{T}}(\mathbf{x}) = [1,x,y,z,xy,xz,yz,x^2,y^2,z^2]$ in 3D), where the points' coordinates are relative to the star point position and normalized with the cloud radius. Assuming $np > m$ in Ω_i, the vector $\boldsymbol{\alpha}$ is determined by minimizing the following Weighted Least-Squares (WLSQ) functional

$$J_i = \sum_{j=1}^{np} w_i(\boldsymbol{x}_j)\left[\hat{\phi}_j - \phi_j\right]^2 = \sum_{j=1}^{np} w_i(\boldsymbol{x}_j)\left[\mathbf{p}^{\mathrm{T}}(\boldsymbol{x}_j)\boldsymbol{\alpha} - \phi_j\right]^2 \tag{2}$$

in which $w_i(\boldsymbol{x}_j) = w(||\boldsymbol{x}_j - \boldsymbol{x}_i||)$ is a compact support weighting function centered on the star point of the cloud (Fixed Least-Squares (FLS)), see [51]. The minimization of Eq. (2) with respect to $\boldsymbol{\alpha}$ leads to the following system of equations

$$\mathbf{A}\boldsymbol{\alpha} = \mathbf{B}\boldsymbol{\phi} \tag{3}$$

where $\mathbf{A}=\mathbf{P}^{\mathrm{T}}\mathbf{W}(\boldsymbol{x})\mathbf{P}$, $\mathbf{B}=\mathbf{P}^{\mathrm{T}}\mathbf{W}(\boldsymbol{x})$, $\mathbf{W}(\boldsymbol{x})=\mathrm{diag}(w_i(\boldsymbol{x}_j))$ and $\mathbf{P}=[\mathbf{p}(\boldsymbol{x}_1), \mathbf{p}(\boldsymbol{x}_2),\ldots \mathbf{p}(\boldsymbol{x}_{np})]^{\mathrm{T}}$. The vector of unknown coefficients can be obtained from Eq. (3) by inverting matrix **A**. Hence, the approximate value of $\phi(\boldsymbol{x})$ at the star point of the cloud (Eq.(1)) is

$$\hat{\phi}(\boldsymbol{x}_i) = \mathbf{p}^{\mathrm{T}}(\boldsymbol{x}_i)\,\mathbf{A}^{-1}\mathbf{B}\,\boldsymbol{\phi} = a_{ij}\phi_j \tag{4}$$

where summation over repeated indices is assumed. Since in the FLS matrices **A** and **B** are constant over Ω_i, the first-order derivatives of $\phi(\boldsymbol{x})$ at $\boldsymbol{x}_i$ are given by

$$\frac{\partial\hat{\phi}(\boldsymbol{x}_i)}{\partial x_k} = \frac{\partial\mathbf{p}^{T}(\boldsymbol{x}_i)}{\partial x_k}\,\mathbf{A}^{-1}\mathbf{B}\,\boldsymbol{\phi} = b_{ij}^{k}\phi_j \tag{5}$$

and higher-order derivatives can be obtained by successive differentiation of the **p** vector (up to the degree of the basis in use).

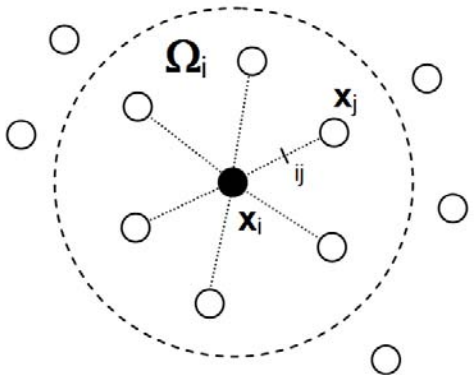

Figure 1. Local approximation domain in the FPM.

It is important to note that the FPM approximation does not interpolate the nodal parameters ϕ_j. These are simply internal values used to construct $\widehat{\phi}(\boldsymbol{x})$, the true approximation for which the governing equations and boundary conditions are enforced. In addition, since the FLS procedure is discontinuous, the metric coefficients in the FPM lack symmetry properties, i.e $\left|b_{ij}^{k}\right| \neq \left|b_{ji}^{k}\right|$. As a result, collocation techniques become a natural choice to discretize the problem equations. Further details about the FPM approximation and the global and local domain discretization techniques employed are given in [51, 52].

2.1 Accuracy of the FPM approximation

The characteristics of the FPM approximation depend to a large extent on the number and distribution of points in the local clouds, the weighting function and the approximation bases chosen; this makes it difficult to obtain theoretical accuracy estimates for general application cases. Nevertheless, studies on simplified models help characterize the behavior of FPM approximations. Using regular 1D point distribution and symmetric clouds without weighting, [53] shows that quadratic approximations (as used in this work) lead to discrete derivatives similar to those obtained with central differences, i.e. second-order space accurate. However, in asymmetric clouds (or irregular point distributions) the accuracy tends to first-order and the effective value attained depends considerably on the weighting function employed. If the locality of the weighting function is increased, the approximation tends to second-order accuracy. Comparable results are shown in [54], where theoretical estimates are obtained using a MLS technique in multidimensional FPM approximations, and [55], which focuses on the effects of the distribution of points. According to these results, second-order accuracy can be considered an upper bound in quadratic FPM approximations, with the attainable value depending on the characteristics of the specific problem being solved. Numerical investigations confirm these results in practical application cases; see grid convergence analyses in [56] and the examples in Section 5.

3 THE FLOW SOLVER

Problems governed by the compressible Euler equations are considered in this work. In conservative differential form these equations can be written as

$$\frac{\partial \mathbf{U}}{\partial t} + \frac{\partial \mathbf{F}^{k}}{\partial x_{k}} = \mathbf{0} \tag{6}$$

where $\mathbf{U} = [\rho, \rho u_i, \rho e_t]^T$ is the conservative variables vector and $\mathbf{F}^k = [\rho u_k, \rho u_i u_k + \delta_{ik} p, \rho e_t + u_k p]^T$ is the advective flux vector in the k^{th} coordinate direction. The variables u_i, ρ, p and e_t denote the fluid velocity components, density, pressure and total energy, respectively; δ_{ik} is the Kronecker delta and the subscripts i,k range from 1 to 3. The equation of state for a perfect gas completes the system (6).

The semi-discrete equations are obtained by replacing the continuous spatial variables with their discrete approximations (Eqs. (4) and (5)). Following [50] the equations (6) are rewritten as

$$\frac{\mathrm{d}\hat{\mathbf{U}}_i}{\mathrm{dt}} = -2\sum_{j\neq i} b_{ij}^k \left[\tilde{\mathbf{F}}_{ij}^k - \tilde{\mathbf{F}}_i^k\right] \qquad \forall\, j \in \Omega_i \tag{7}$$

where $\hat{\mathbf{U}}_i = a_{ij}\mathbf{U}_j$ is a discrete approximation of the conservative variables at the star point $\boldsymbol{x}_i$, $\tilde{\mathbf{F}}_i^k = \mathbf{F}^k(\mathbf{U}_i)$ is the k^{th} component of the convective flux vector and $\tilde{\mathbf{F}}_{ij}^k$ are numerical fluxes at the midpoint of the edge connecting $\boldsymbol{x}_i$ to another point $\boldsymbol{x}_j$ in Ω_i. This form enables easy introduction of convective stabilization into the numerical scheme. The approximate Riemann solver of Roe [57] is employed in this work. This leads to

$$\tilde{\mathbf{F}}_{ij}^k = \tfrac{1}{2}\left(\tilde{\mathbf{F}}_j^k + \tilde{\mathbf{F}}_i^k\right) - \tfrac{1}{2}\left|\mathbf{A}_{\hat{n}}(\mathbf{U}_i, \mathbf{U}_j)\right|\left(\mathbf{U}_j - \mathbf{U}_i\right)\hat{n}_{ij}^k \tag{8}$$

where $\hat{\boldsymbol{n}}_{ij}$ is a unit vector in the direction of the edge $\boldsymbol{l}_{ij} = \boldsymbol{x}_j - \boldsymbol{x}_i$ and $\left|\mathbf{A}_{\hat{\boldsymbol{n}}}(\mathbf{U}_i, \mathbf{U}_j)\right|$ is the positive Roe matrix in the same direction [58]. To increase the spatial accuracy of the scheme, the variables $\mathbf{U}_i$ and $\mathbf{U}_j$ in Eq. (8) are replaced with higher-order reconstructions obtained by slope-limited MUSCL extrapolation [49] with Van Albada limiter [59].

A multi-stage time marching discretization scheme is used for Eq. (7). The problem solution is advanced from a time level t^n to a level t^{n+1} by

$$\hat{\mathbf{U}}_i^{(m)} = \hat{\mathbf{U}}_i^{(m-1)} - \alpha_m \Delta t_i \mathbf{RHS}_i\left(\mathbf{U}_j^{(m-1)}\right) \quad m = 1, s \tag{9}$$

where $\hat{\mathbf{U}}_i^{(0)} = \hat{\mathbf{U}}_i^{(n)}$, $\hat{\mathbf{U}}_i^{(s)} = \hat{\mathbf{U}}_i^{(n+1)}$, α_m are suitable integration coefficients [60] and $\mathbf{RHS}_i(\cdot)$ is the right-hand side of Eq. (7) with the fluxes evaluated at stage $(m-1)$. Local time stepping and implicit residual averaging [61] are used to accelerate the convergence to the steady state. Since $\mathbf{RHS}_i(\cdot)$ in Eq. (9) depends on the internal nodal values $\mathbf{U}_j$, a non-symmetric linear system has to be solved at the end of each time integration stage to recover $\mathbf{U}_j$ from the updated approximate solution $\hat{\mathbf{U}}$. From Eq. (4), this system is

$$\sum_{\forall j \in \Omega_i} a_{ij} \mathbf{U}_j = \hat{\mathbf{U}}_i \quad i = 1, n \tag{10}$$

and can be solved inexpensively with a small number of Gauss-Seidel iterations.

4 THE MESHLESS ERROR ESTIMATE

Among the sources of error affecting the accuracy of a numerical solution, the discretization error plays a major role. This error, which depends on the underlying discretization and the characteristics of the numerical scheme, is typically defined as

$$\mathrm{e}_h = \phi - \phi_h \tag{11}$$

where ϕ denotes the exact solution of the continuous problem $L(\phi)=0$, and ϕ_h the exact solution of its discrete counterpart, $L_h(\phi_h)=0$, computed on a grid with characteristic size h (iterative and round-off errors are considered to be zero). Assuming that the discrete problem operator L_h is linear (or has a linearized form) and applying it to Eq. (11), the following equation for the discretization error is obtained

$$L_h(\mathrm{e}_h) = L_h(\phi) - L_h(\phi_h) = L_h(\phi) - 0 = L_h(\phi) \tag{12}$$

Eq. (12) can be solved with the same approximate method used to obtain the discrete solution, but with an extra source term responsible for the local generation and destruction of error in the domain. The equivalence between $L_h(\cdot)$ (discrete differential residual) and the truncation error (τ_h) can be obtained from the following relation between the differential operators [18]

$$L(\cdot) = L_h(\cdot) + \tau_h(\cdot) \tag{13}$$

where $(\cdot)$ denotes an arbitrary problem solution. Introducing ϕ in Eq. (13) the term $L(\phi)$ vanishes, and substituting the result into Eq. (12) yields

$$L_h(\mathrm{e}_h) = -\tau_h(\phi) \tag{14}$$

which is the basis of methods using DET equations. As neither the truncation error nor the exact solution are known in practice, approximations are typically used to solve Eq. (14).

With the objective to identify local discretization errors with minimum computational overhead, a surrogate measure of e_h is proposed following the results in [20]. There, using central differences in a 1D steady diffusion problem, the authors show that e_h in Eq. (14) is proportional to the local truncation error. Hence, by equivalence between central differences

and FPM discretizations on regular 1D clouds (see Section 2.1 and the proof in [53]), we assume that locally $e_h \propto \tau_h$ and the latter is obtained by inserting ϕ into Eq. (13). This gives

$$e_h \propto \tau_h(\phi) = -L_h(\phi) = -R_h(\phi) \tag{15}$$

where $R_h(\cdot)$ is the discrete differential residual of the problem.

In the context of the compressible Euler equations, $R_h(\cdot)$ in Eq. (15) can be obtained from a discrete (simplified) form of Eq. (7), with the exact solution ϕ replaced by an accurate estimate $\mathbf{U}^*$. In this way, the local surrogate error proposed is

$$\mathbf{e}_{\tau_i} = \left|\mathbf{R}_h^i\left(\mathbf{U}^*\right)\right| = \left|\frac{\Delta \mathbf{U}_i^*}{\Delta t} + \sum_j b_{ij}^k \mathbf{F}^k\left(\mathbf{U}_j^*\right)\right| \qquad \forall\, j \in \Omega_i \tag{16}$$

where $\mathbf{F}^k$ is the *k*-component of the convective flux vector and $\boldsymbol{b}_{ij}$ are the metric approximation coefficients of the cloud Ω_i. A global measure of the numerical error over the whole domain is obtained from the local error vector (16) using the following L_2-norm

$$\left\|\mathbf{e}_\tau\right\| = \left(\frac{1}{n}\sum_i \left(\mathbf{e}_\tau^2\right)_i\right)^{1/2} \tag{17}$$

with *n* denoting the total number of points in the computational domain.

Note that the discrete residual $\mathbf{R}_h$ used to calculate the surrogate error (Eq. (16)) does not include the dissipative term arising from the upwind flux discretization in Eq. (7). Numerical tests have shown that this simplification, which reduces computational cost, has no negative effects on the performance of the surrogate error. If the flow is smooth, the dissipation term has no appreciable effects on the solution or indicator; in contrast, near flow discontinuities, dropping the artificial diffusion reduces the smoothing of the solution, sometimes increasing the sensitivity of the indicator to small flow features. In general, tests show that the dissipation terms can safely be omitted in Eq. (16), achieving a considerable reduction in computational cost.

4.1 Computing accurate solution estimates

The solution estimates required in Eq. (16) are calculated through a modified form of the local FPM approximation (Eq. (4)), by using the partition of unity property and scaling by a half the stencil of points surrounding $\boldsymbol{x}_i$ (see [50]). This results in

$$\phi_i \approx \phi_i^* = \hat{\phi}_i + 2\sum_{i \neq j} a_{ij}\left(\overline{\phi}_{ij} - \hat{\phi}_i\right) \tag{18}$$

where $\widehat{\phi}$ are the values of the original solution at the cloud points and $\overline{\phi}_{ij}$ are samples of the solution at the midpoint of the rays connecting $\boldsymbol{x}_i$ with its neighbors. Note that Eq. (18) reduces by a half the local grid size; thus the accuracy of the approximation can be improved as long as the reconstructed solution is accurate enough (convergence rate is the same). These values will be obtained by higher-order reconstruction of the original solution around $\boldsymbol{x}_i$. The stencil of points used is larger than in the original solution. Due to the reconstruction procedure used to derive the improved values (see section 4.1.1), the support of the enhanced solution typically includes three layers of neighbors around point $\boldsymbol{x}_i$ vs. only two for the original solution. Therefore, more accurate solution samples are expected from the increased support. The improvement in accuracy achieved in practice will be numerically investigated in Section 4.2

The approach adopted to calculate the samples $\bar{\phi}_{ij}$ is inspired on slope-limited geometric methods [62]. These techniques reconstruct the solution between two points $\boldsymbol{x}_i$ and $\boldsymbol{x}_j$ by fitting higher-order interpolators on an enlarged spatial support, and require the use of non-linear limiters to avoid spurious oscillations across discontinuities. Since this step can contaminate the recovered solution field and generate dependence on the limiter function chosen (see [63]), a more robust approach is proposed in the next section.

Note that ϕ_i^* could also be obtained by using higher-order schemes [33-35]. Since this approach is attractive in a meshless context, a preliminary investigation was conducted. The results were satisfactory, but the implementation was not deemed cost-effective, and some lack of robustness was also observed (especially in 3D problems). Nevertheless, further investigation is required on this issue.

4.1.1 ENO piecewise polynomial reconstruction

Essential non-oscillatory schemes (ENO) [64] are a family of reconstruction methods in which the solution interpolant is chosen between the smoothest of piecewise polynomials computed for the same sampling location on different local supports (stencils). As the selection procedure adopted prevents interpolation across discontinuities, limiting is no longer necessary. ENO schemes have also interesting properties, such as conservation of the mean, and guarantee total variations bounded by the truncation error of the reconstruction. Improvements to the basic ENO technique have been also proposed to solve certain deficiencies concerning the need of large stencils (difficult to obtain in unstructured

discretizations) and the lack of accuracy in smooth data reconstruction problems; see for instance Weighted-ENO (WENO) [65] and Hermite-WENO (HWENO) [66] methods.

In this work a standard ENO technique is employed to compute the $\overline{\phi}_{ij}$ samples required in Eq. (18). Thus, the enhanced solution field is reconstructed in the interval $\mathbf{I}_i = [\mathbf{x}_{i-1/2},\mathbf{x}_{i+1/2}]$ (in the direction of the edge $\boldsymbol{l}_{ij} = \boldsymbol{x}_j - \boldsymbol{x}_i$) by one of the following central, left or right-biased quadratic interpolation polynomials [67]

$$\begin{aligned} p_{i-1}(x') &= \hat{\phi}_i - \frac{D_{i-1}}{24} + x'\left[d_{i-1/2} + \frac{D_{i-1}}{2}(x'+1) \right] \\ p_i(x') &= \hat{\phi}_i - \frac{D_i}{24} + x'\left[d_i + \frac{D_i}{2}x' \right] \\ p_{i-1}(x') &= \hat{\phi}_i - \frac{D_i}{24} + x'\left[d_{i+1/2} + \frac{D_{i+1}}{2}(x'-1) \right] \end{aligned} \tag{19}$$

where $\hat{\phi}_i$ is the original discrete solution at $\boldsymbol{x}_i$, $d_{i+1/2} = \hat{\phi}_{i+1} - \hat{\phi}_i$ and $D_i = d_{i+1/2} - d_{i-1/2}$ are the first and second differences respectively; $d_i = (d_{i+1/2} + d_{i-1/2})/2$ and $0 \le x' \le 1$ is a non-dimensional length parameter along $\boldsymbol{l}_{ij}$. In order to evaluate first and second differences, the discrete solution at fictitious sampling points $\boldsymbol{x}_{j+1}$, $\boldsymbol{x}_{i-1}$ and $\boldsymbol{x}_{i-2}$ in the direction of the edge is required (see Figure 2). These values are obtained by means of the following central and 2nd-order backward finite difference approximations

$$\begin{aligned} \hat{\phi}_{i-1} &\approx \hat{\phi}_j - 2\boldsymbol{l}_{ij} \cdot \nabla\hat{\phi}_i \\ \hat{\phi}_{j+1} &\approx \hat{\phi}_i + 2\boldsymbol{l}_{ij} \cdot \nabla\hat{\phi}_j \\ \hat{\phi}_{i-2} &\approx 4\hat{\phi}_{i-1} - 3\hat{\phi}_i + 2\boldsymbol{l}_{ij} \cdot \nabla\hat{\phi}_i \end{aligned} \tag{20}$$

where the solution gradients are computed from the original FPM solution using Eq. (5).

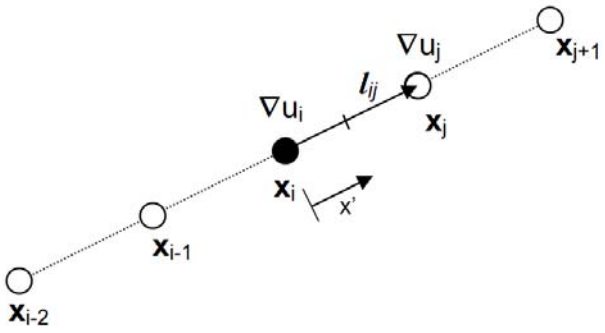

Figure 2. Stencil of points employed for cubic ENO reconstruction around $\boldsymbol{x}_i$ in the direction of $\boldsymbol{l}_{ij}$.

The interpolation polynomial reconstructing the enhanced solution field between $\boldsymbol{x}_{i-1/2}$ and $\boldsymbol{x}_{i+1/2}$ is chosen following standard ENO practice

$$
\begin{aligned}
&\text{if } |d_{i-1/2}| \le |d_{i+1/2}| \text{ then} \\
&\quad \text{if } |D_{i-1}| \le |D_i| \text{ then } p_{i-1}(x') \text{ else } p_i(x') \\
&\text{else} \\
&\quad \text{if } |D_i| \le |D_{i+1}| \text{ then } p_i(x') \text{ else } p_{i+1}(x') \\
&\text{endif}
\end{aligned}
\tag{21}
$$

and the midpoint samples required in Eq. (18) are obtained from

$$
\overline{\phi}_{ij} = p_k\left(x'=1/2\right) \tag{22}
$$

where k can take the values $i-1$, i or $i+1$ depending on the polynomial chosen in (21). Note that Eqs. (19) allow a continuous reconstruction of the unknown function in the interval $[\mathbf{x}_{i-1/2},\mathbf{x}_{i+1/2}]$ and this fact enables the use of a different cloud scaling in Eq. (18). The numerical tests performed showed little influence on the accuracy of ϕ_i^* (esta no entiendo qué significa).

4.2 Numerical tests

The accuracy and convergence of the improved solution estimate (Eq. (18)) is investigated by evaluating the effectivity index in several test cases. This parameter is defined as [68]

$$
\theta = \bar{e}/e \tag{23}
$$

where $\bar{e} = \|\phi^* - \widehat{\phi}\|$ is the error norm of the original FPM approximation (Eq. (4)) referenced to the improved estimate and $e = \|\phi - \widehat{\phi}\|$ is the exact error norm. As mentioned in Section 2.1, the convergence characteristics of the FPM can depend (particularly in 3D problems) on the geometry of the clouds and the weighting functions employed. Hence, in the examples presented these effects are minimized using similar settings of the FPM approximation, regular point discretizations and a uniform scaling between the models.

The first example involves the approximation of a smooth Gaussian function defined in a one-dimensional domain [0,1]

$$
f(x) = ae^{-(x-b)^2/2c^2} \tag{24}
$$

where $a=4/\pi\delta$, $b=0.5$, $c^2=2\delta$ and $\delta=0.005$. To study the convergence of the effectivity index, the coarser grid used has uniform point distribution with spacing $h=0.125$, and finer discretizations are generated by halving h. The errors in Eq. (23) are computed in L_2-norm and a complete quadratic polynomial basis is used in clouds with $np=5$. Both the standard FPM approximation and the higher-accuracy approximation are displayed in Figure 3, along

with the evolution of the effectivity index. The plots show that a noticeably improved approximation is obtained with Eq. (18). Convergence to the exact solution is also demonstrated by the evolution of the effectivity index.

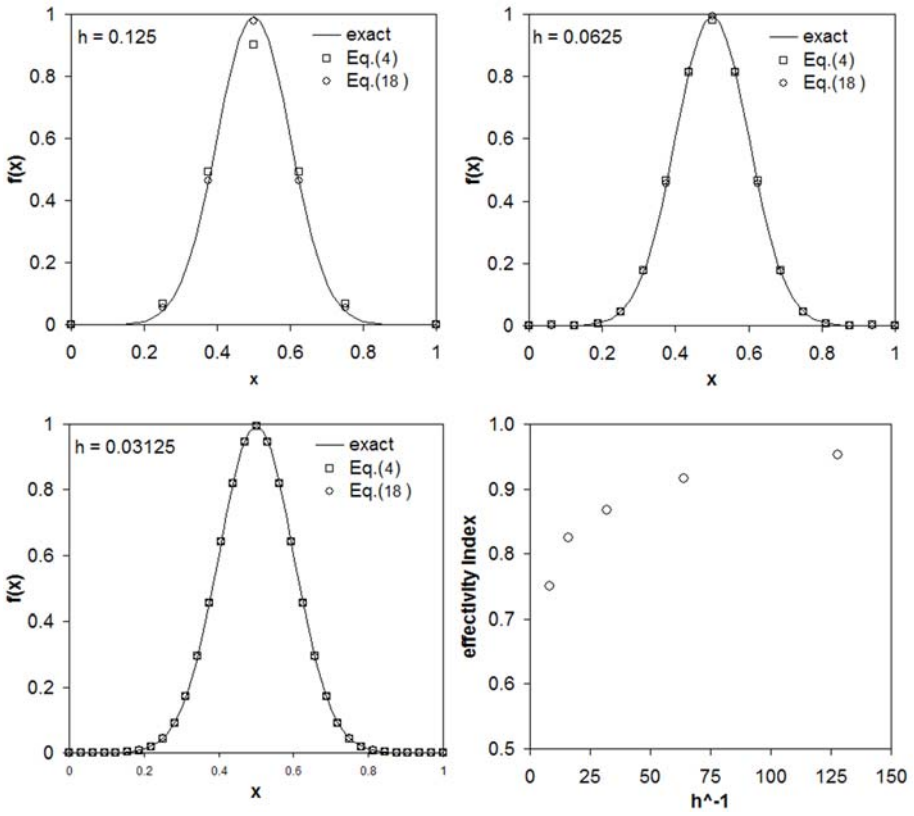

Figure 3. Approximation of a smooth Gaussian function in a one-dimensional domain.

A similar setup is employed in the second example, but this time a sign discontinuity is introduced in the Gaussian test function. The results show improved approximation for the higher-accuracy estimate (Figure 4), but no asymptotic convergence of the effectivity index. This happens because the approximation near the discontinuity reverts to O(h), thus hampering the convergence of the global error estimate.

The next two examples investigate the performance of the estimate (18) in 3D problems. The following test function is adopted in a cubic analysis domain $[0,1]^3$

$$f(x,y,z) = 64x(1-x)y(1-y)z(1-z) \tag{25}$$

The initial discretization consists of an unstructured distribution of 1527 points (h≈0.1) and successive refined discretizations are obtained by halving the point spacing. Complete quadratic polynomial bases in clouds with np=30 are employed. As observed in Figure 5, convergence of the improved estimate is also achieved in this example.

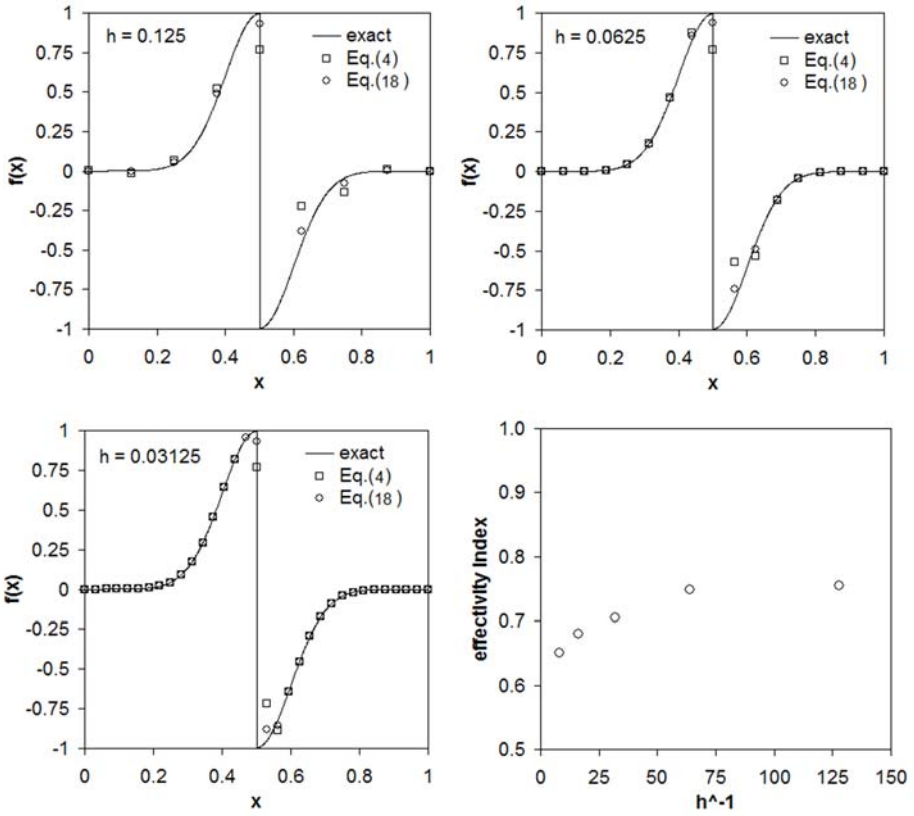

Figure 4. Approximation of a one-dimensional Gaussian function with a sign discontinuity.

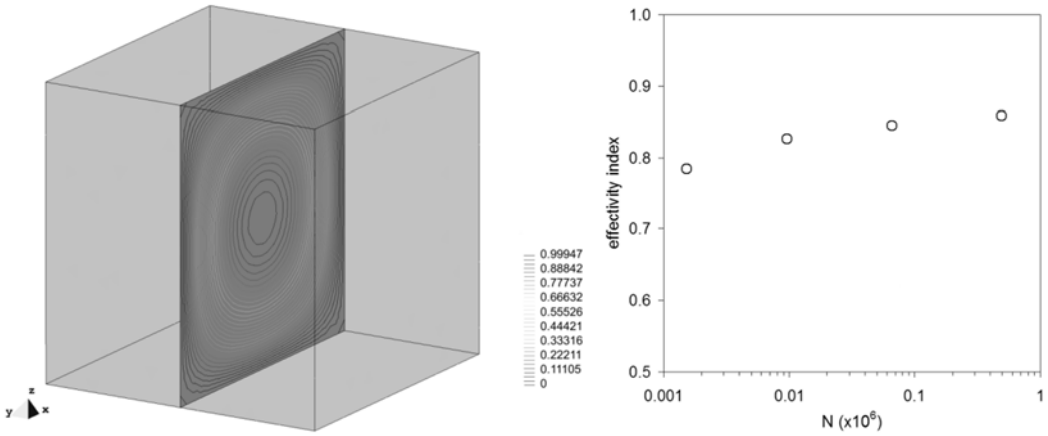

Figure 5. Behavior of the approximation error for a smooth three-dimensional function.

Finally, mirroring the 1D examples, a sign discontinuity at x=0.5 is introduced in the test function. The results in Figure 6 show a satisfactory accuracy of the solution estimate but, like the one-dimensional case (Figure 4), the discontinuity affects both the global approximation error and its convergence rate. Overall, the behavior observed in the tests indicates the ability of the proposed methodology to obtain an improved estimate of the exact solution, as required to compute the surrogate local error (16).

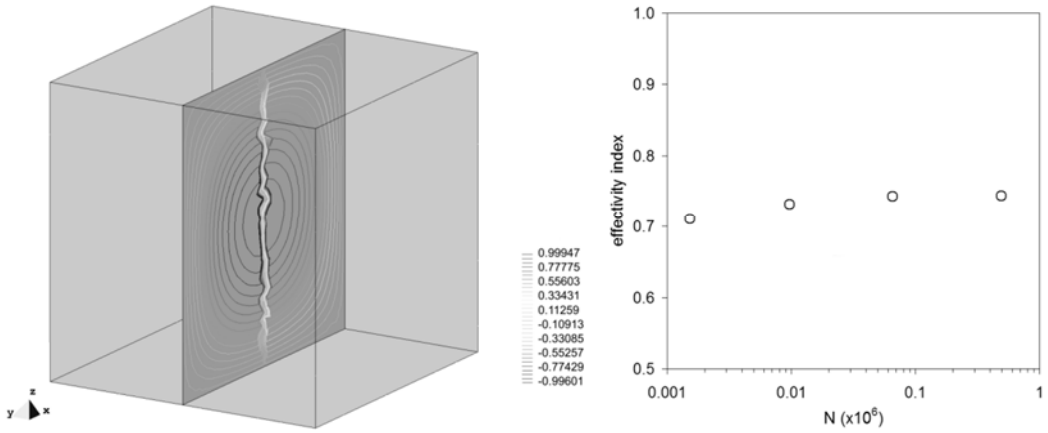

Figure 6. Behavior of the approximation error for a three-dimensional function with a sign discontinuity.

5 APPLICATIONS TO ADAPTIVE COMPRESSIBLE FLOW PROBLEMS

The proposed error estimate is now applied to compressible inviscid flow problems. Its performance and suitability to guide grid adaptation procedures is investigated in comparison with reference error estimates and typical feature-based flow sensors.

5.1 NACA 0012 airfoil

This example involves the 2D flow around a NACA 0012 airfoil. Four discretizations with characteristic point spacings $h_1<h_2<h_3<h_4$ are generated from a coarse model (h_4) by scaling the grid sizes uniformly. This way, discretizations ranging from 2487 to 5836 nodes are obtained with an average refinement ratio $r = h_{k+1}/h_k \approx (n_{k+1}/n_k)^{-1/2} = 1.15$. The simulation conditions involve different freestream Mach numbers and angles of attack, namely: M=0.3 at α=1.25º and 4º and M=0.8 at α=0º, 1.25º and 4º. The boundary conditions applied are freestream Riemann conditions on the outer domain boundary and slip conditions on the airfoil surface. The numerical solutions use third-order MUSCL extrapolation with Van Albada limiter and a 4-stage time marching scheme. The FPM discretization uses a complete quadratic approximation basis in clouds with 15-21 points.

For each test case, the observed order of accuracy of the scheme is computed by Richardson's extrapolation using the three finest discretizations. The values obtained range between 1.54 and 1.87, with mean **p=1.74**. This averaged convergence rate is assumed to be representative of the true discretization error of the problem. As shown in Figure 7, the convergence rates of the density ($e_{\tau 1}$), momentum ($e_{\tau 2,3}$) and energy ($e_{\tau 4}$) components of the surrogate error estimate (16) are close to the prediction of Richardson's method. This shows a satisfactory relationship between the proposed indicator and the problem discretization error.

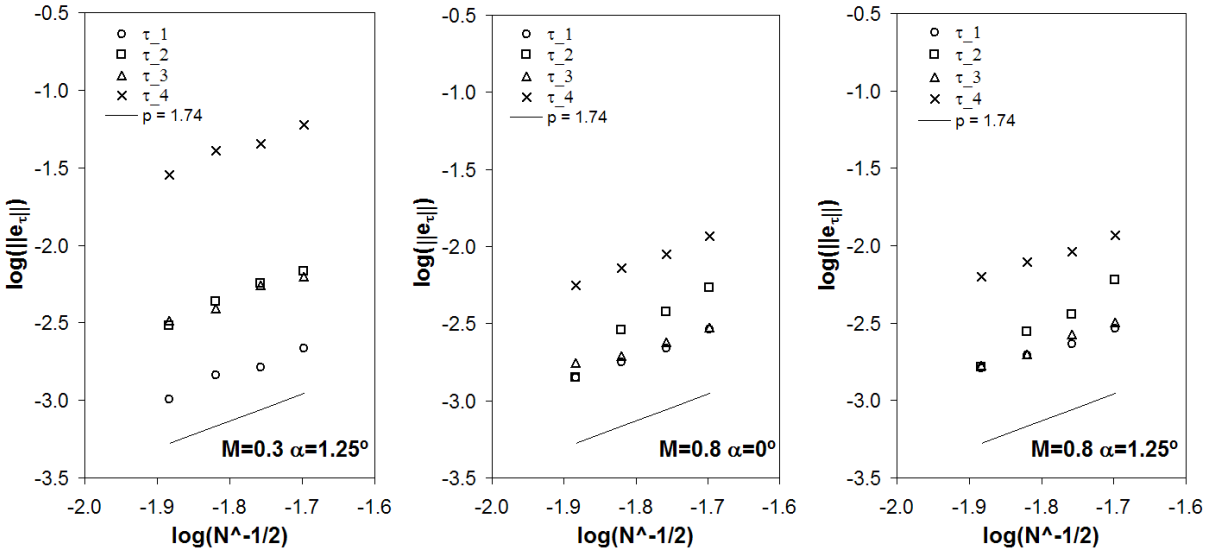

Figure 7. Convergence of the components of the global truncation error-based estimate (density ($e_{\tau 1}$), momentum ($e_{\tau 2,3}$) and energy ($e_{\tau 4}$)) computed for the NACA 0012 airfoil problem.

Regarding the iterative convergence of Eq. (17), the test cases analyzed showed that the truncation error-based global estimate converges after a short initial transitory, and faster than the flow field (results are not reported here). This fact, suggesting that the contribution of the underlying discretization (resolution and quality) to the truncation error prevails over the contribution of the flow solution itself, could be advantageous. This happens because surrogate error measures based on the approximate solution can be obtained early in the iterative process, even before full solution convergence is achieved. However, a reduced sensitivity of the estimate to the solution features may cause a lack of correlation with errors in variables of practical interest. Pros and cons should be carefully analyzed.

The suitability of the local error estimate (16) to drive grid adaptation is studied next by comparison with a typical feature-based sensor relying on the solution curvature

$$r_i = \sum_{j=1}^{n_{nei}} \left| \boldsymbol{l}_{ij} \cdot \left(\nabla \phi_j - \nabla \phi_i \right) \right| \quad \forall\, j \in \Omega_i \tag{26}$$

The target variable chosen is the fluid density and the adaptive strategy follows the guidelines of [69]. Hence, a nodal refinement indicator is first calculated at each point with

$$\varphi_i = \log\left(\frac{1}{r_i} \frac{1}{np} \sum_{j=1}^{np} r_j \right) \tag{27}$$

where np is the number of points in the cloud of $\boldsymbol{x}_i$ and r_j depends on the sensor chosen. It is calculated with Eq. (26) for feature-based detection, or it corresponds to the density component of vector (16) at $\boldsymbol{x}_j$ when the surrogate error is used. Once the refinement indicator

is calculated, its mean φ_m and standard deviation s_φ are used to determine clouds which require refinement or coarsening. The star point $\boldsymbol{x}_i$ is tagged for refinement when $\varphi_i > \varphi_m + N_{ref} s_\varphi$ and, conversely, the point $\boldsymbol{x}_i$ is marked for removal if $\varphi_i < \varphi_m - N_{rem} s_\varphi$. Thus, local spikes of the error are put back in line with the mean across the domain, which is dominated by smooth flow regions. The thresholds used here are $N_{ref} = 1$ and $N_{rem} = 0$. These values have proved satisfactory for a wide range of inviscid compressible flow problems.

The test case involves an inviscid flow with M=0.8 and α=1.25º. The initial discretization consists of an unstructured distribution of 2674 points and four refinement levels are performed. The first one is triggered after achieving solution convergence on the initial coarse grid and additional refinement passes are performed subsequently, ensuring the convergence of the intermediate solutions. A close-up of the initial and final adapted discretizations is shown in Figure 8. The finest discretization for the truncation error-driven procedure has 6165 points, versus 7105 for the feature-based indicator. The truncation error-based indicator not only concentrates new points around sharper solution features but also near the airfoil surface and the wake; two zones mostly ignored by the curvature-based detector.

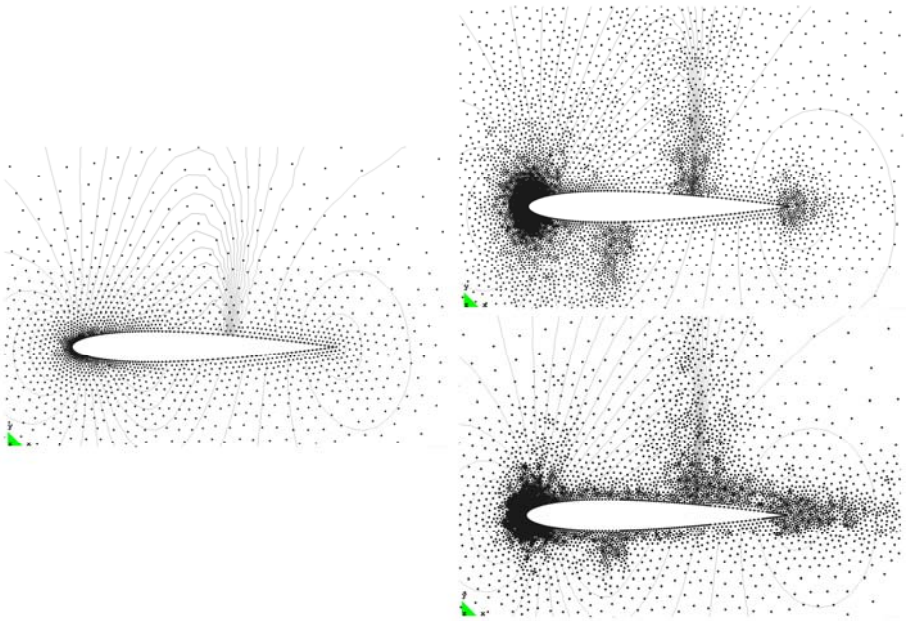

Figure 8. Initial coarse (left) and final adapted discretizations (right): curvature-based adaptivity (top) and truncation error-based adaptivity (bottom). NACA 0012 airfoil, M=0.8 and α=1.25º.

Figure 9 shows the convergence with grid refinement of the aerodynamic normal force error (C_{Nh}) and the global estimate (17). The force error is computed relative to a grid-converged result (C_{Nf}) obtained on a very fine uniform discretization (n=15021). The results show that a lower error in the aerodynamic force is obtained with the truncation error-based indicator

(Figure 9 left), although the convergence rates observed for both methods are quite similar. Regarding the global error estimate (Figure 9 right), its magnitude decreases with the grid size at a rate close to the order of accuracy of the scheme, but the convergence slows down slightly after the second refinement stage. This effect is more notorious when the curvature-based indicator is used (probably due to a more localized refinement).

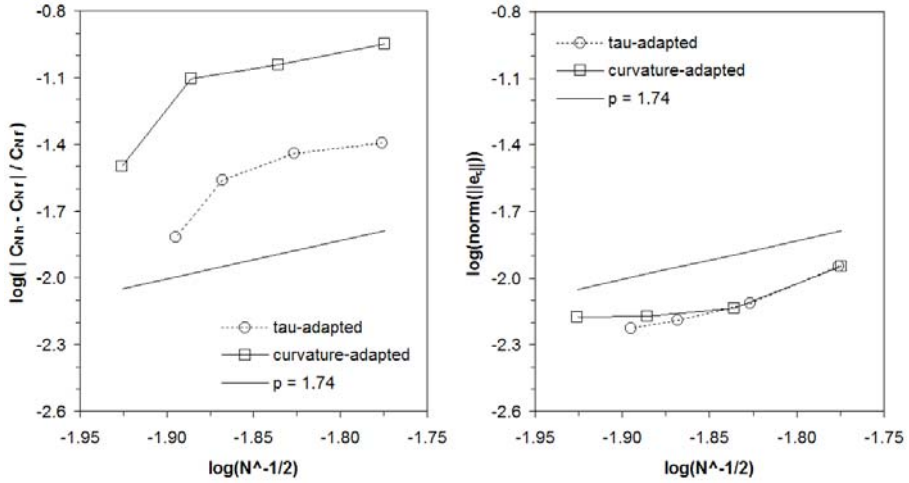

Figure 9. Behavior of the normal force error (left) and the numerical error estimate (right) with the grid refinement (norm($\|\mathbf{e}_\tau\|$) is the norm of the global error vector (17)). NACA 0012 airfoil, M=0.8 and α=1.25º.

The pressure distributions calculated for the initial and final adapted discretizations are compared in Figure 10. The truncation error-driven adaptivity resolves the upper shock better than the feature-based procedure (possibly due to a higher and more uniform density of points added near the airfoil) but the shock on the lower side of the airfoil is not well resolved. As mentioned before, this could reflect a reduced sensitivity of the proposed indicator to the flow features (particularly weaker ones). At the leading and trailing edges both indicators achieve similar results, comparable to the reference solution (15021 points).

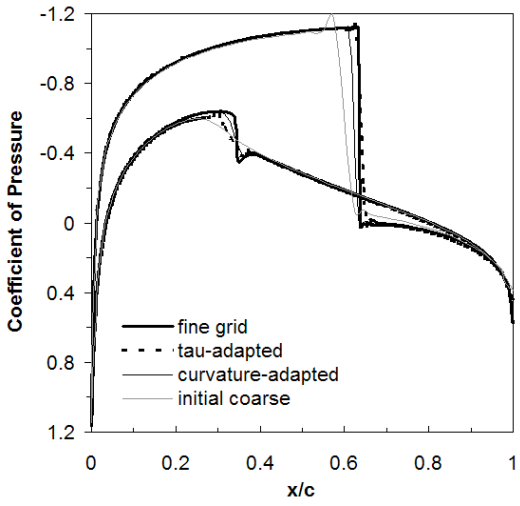

Figure 10. Comparison of the pressure distributions obtained from the adapted flow solutions and the fine reference discretization. NACA 0012 airfoil, M=0.8 and α=1.25º.(Las 2 líneas delgadas no se distinguen bien)

5.2 NACA wing-body configuration

The proposed error estimate is applied below to the transonic flow over a NACA wing-body configuration [70] (Figure 11) and the results are compared with Richardson's extrapolation. To this effect, four model discretizations with point spacings $h_1<h_2<h_3<h_4$ are generated from a coarse model (h_4) by scaling the grid sizes in a uniform manner. The discretizations range from 427000 to 2860318 nodes with 83162 to 694482 boundary triangles respectively. The averaged refinement ratio is $r = h_{k+1}/h_k = (N_{k+1}/N_k)^{-1/3} = 1.235$. Figure 12 shows a close view of the surface discretization near the wing tip.

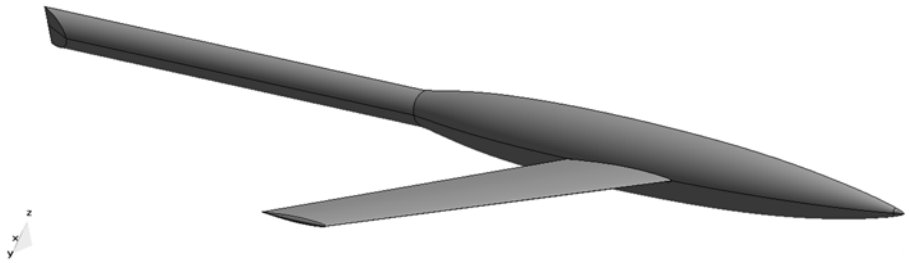

Figure 11. Analysis test model NACA RM L51F07.

The flight conditions chosen are M=0.9 with angles of attack α=1 and 4º. The boundary conditions are flow symmetry on a plane along the fuselage centerline, freestream Riemann conditions on the outer boundary and slip conditions on the body surface. The solution scheme is similar to that used in the previous test cases. The FPM approximation uses a complete quadratic basis on clouds with 30-50 points. As mentioned, Richardson's extrapolation is used to obtain the higher-order estimates of the aerodynamic forces used to calculate the solution error. The observed order of accuracy of the scheme is **p=1.69** for α=1º and **p=1.41** for α=4º.

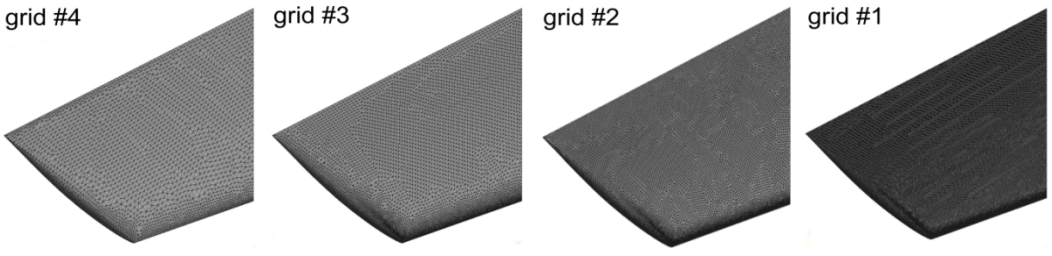

Figure 12. View of the boundary discretization near the wing tip for grids 1-4.

The convergence of the global error estimate (17) is examined in Figure 13 for the different components of the truncation error. The convergence rates obtained are close to that predicted by Richardson's extrapolation. Similar to the 2D case, an early iterative convergence of the proposed error estimate was also observed in this case (results are not reported here).

The error estimate (16) is used next to drive *h*-adaptation and the results are compared with those from the conventional feature-based indicator (26). The freestream Mach number is M=0.9 and the body angle of attack is α=4º. The initial domain discretization consists of an unstructured distribution of 606756 points and 174812 boundary triangles. Four refinement levels are performed during the adaptive simulation and the settings of the adaptive procedure are similar to those used in the previous example.

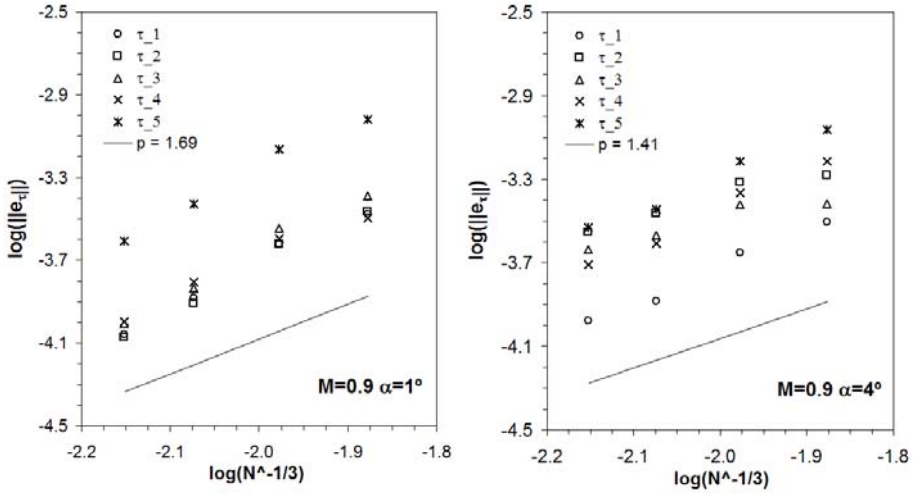

Figure 13. Convergence of the truncation-error based estimate for the NACA wing-body test case (density ($e_{\tau 1}$), momentum ($e_{\tau 2,3,4}$) and energy ($e_{\tau 5}$)).

The level of refinement achieved with both error indicators is very similar. The truncation error-driven procedure attains 1001624 points and 198822 boundary triangles, while 1041624 points and 205320 triangles are obtained with the curvature-based indicator. The evolution of normal force error (computed with respect to the extrapolated value C_{Ne}) and the global error estimate (17) during the adaptive computation is shown in Figure 14. Like the previous test case, the truncation error-based indicator leads to a lower error. The convergence rates and the reduction of the surrogate error estimate (17) achieved are quite similar for both indicators.

Pressure distributions along two wing spanwise stations are shown in Figure 15 together with experimental and reference results from the finest grid model. Both error indicators lead to similar results around the main flow features. Figure 16 shows the adapted discretizations. As observed in the previous test case, feature-based adaptivity appears more effective around weaker flow discontinuities (e.g the shock on the fuselage) but truncation error adaptivity refines in areas where the flow field is smoother (trailing edge and wing tip), probably contributing to the more effective reduction of the force errors shown in Figure 14.

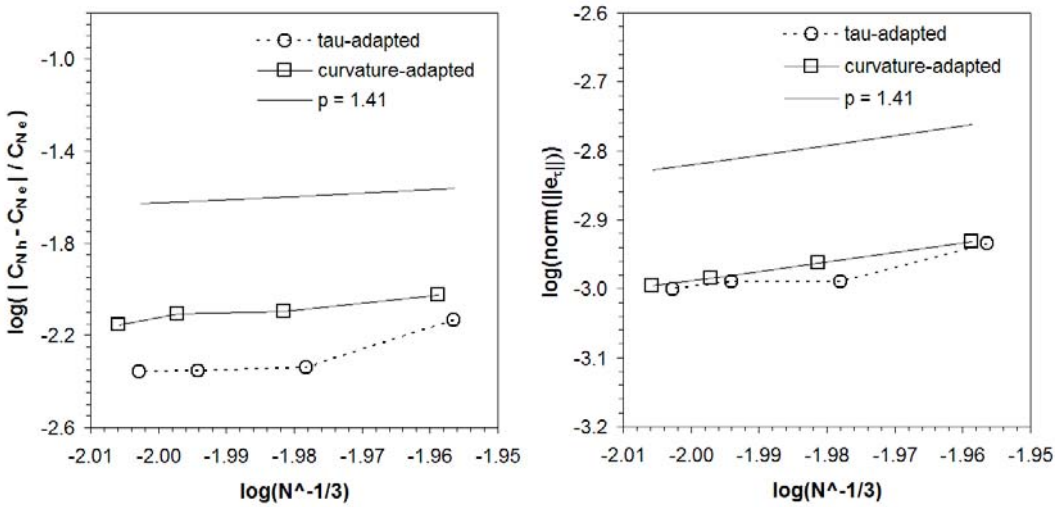

Figure 14. Behavior of the normal force error (left) and the numerical error estimate (right) with the grid refinement. (norm($\|\mathbf{e}_\tau\|$) denotes the norm of the global error vector (17)). NACA wing-body, M=0.9 and α=4º.

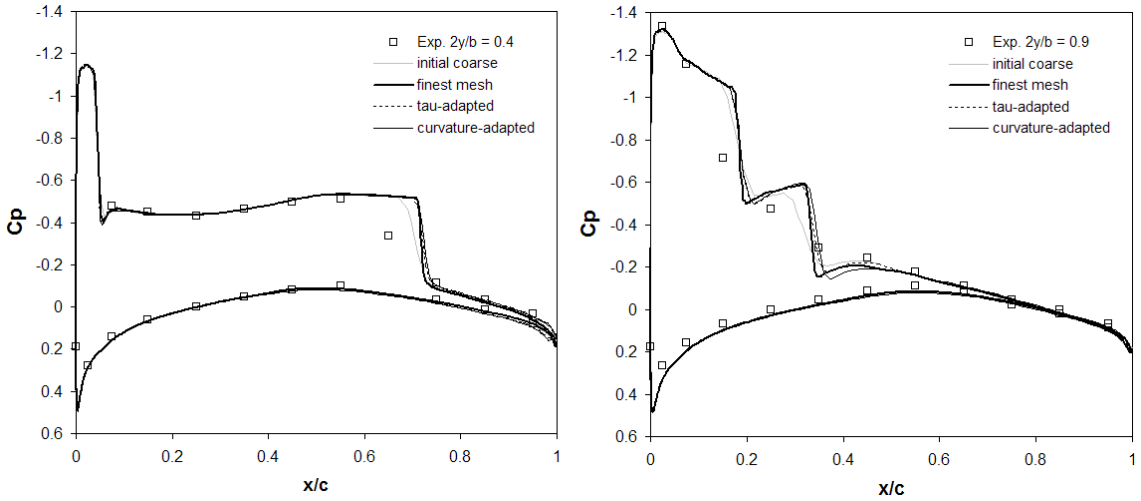

Figure 15. Comparison of pressure distributions obtained with the final adapted flow solutions and the finest reference discretization. NACA wing-body, M=0.9 and α=4º.

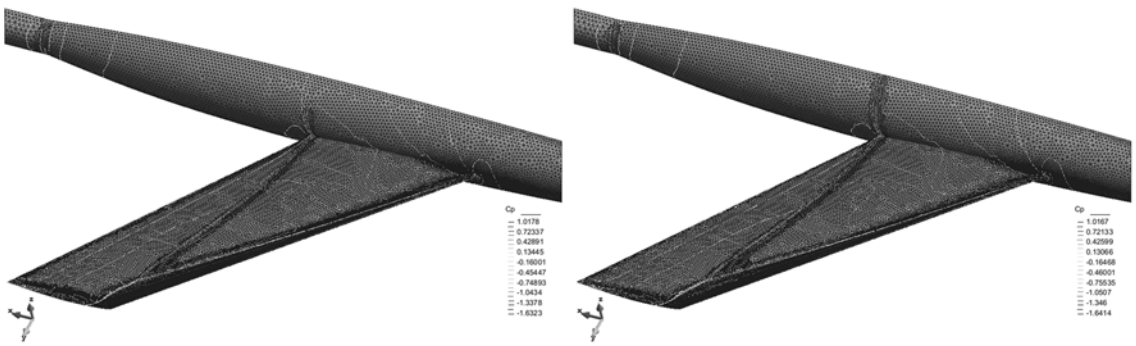

Figure 16. Final adapted boundary discretizations obtained with the truncation error-based indicator (left) and the curvature-based indicator (right). NACA wing-body, M=0.9 and α=4º.

6 CONCLUSIONS

An *a-posteriori* error estimate based on an approximate form of the truncation error terms has been presented in this work. The methodology is implemented in the framework of the

meshless Finite Point Method, although the formulation could be easily extended to other conventional discretization techniques with minor modifications. The proposed error estimate is a surrogate measure of the discretization error obtained from an approximation to the truncation terms of the governing equations. This approximation is calculated from the discrete nodal differential residuals using a reconstructed solution field on a modified stencil of points. To this end, a standard ENO technique is used. It is important to note that the proposed error estimate is designed to be calculated with very low overheads using data structures and information generally available in CFD codes.

The applications of the truncation error-based estimator in this work focus on identification of local and global errors in compressible flow problems. Regarding the global behavior of the indicator, its relation with the problem discretization error was first analyzed using reference values obtained by Richardson's extrapolation. In all the test cases studied the proposed estimate correlates well with the discretization error, with convergence rates close to the observed order of accuracy of the scheme. The relatively fast convergence of the estimate is also worth mentioning, as it delivers fast surrogate error measures without complete flow field convergence. As far as the local behavior of the truncation error-based estimate is concerned, its suitability to guide adaptive procedures has also been examined. Compared with a typical curvature-based indicator, the results show that truncation error-driven adaptivity reduces the problem discretization error more effectively. This was reflected both in lower aerodynamic force error and the evolution of the surrogate numerical error estimate. Moreover, the adapted point distributions seem more uniform when using the truncation error-based indicator, although a small loss of sensitivity to weaker flow features can be observed. Overall, the performance of the proposed local error indicator was considered satisfactory.

Future research is planned on the ability of truncation error-based estimates to provide error bounds for variables of engineering interest in practical applications. In this respect, methods based on numerical imbalance arguments suggest interesting alternatives, e.g. [9, 11].

ACKNOWLEDGMENTS

Part of this work was developed within the ALEF (Aerodynamic Loads Estimation at Extremes of the Flight Envelope) project under the European Commission's 7th Framework Programme (contract number ACP7-GA-2009-211785). The authors gratefully acknowledge the support provided.

REFERENCES

1. Roache, P.J., *Quantification of uncertainty in computational fluid dynamics.* Annual Review of Fluid Mechanics, 1997. **29**: p. 123-160.
2. Oberkampf, W.L. and T.G. Trucano, *Verification and validation in computational fluid dynamics.* Progress in Aerospace Sciences, 2002. **38**: p. 209-272.
3. Roy, C.J., *Review of code and solution verification procedures for computational simulation.* Journal of Computational Physics, 2005. **205**: p. 131-156.
4. Thacker, B.H., et al., *Concepts of model verification and validation.* Los Alamos National Laboratory, LA-14167-MS 2004.
5. Zienkiewicz, O.C. and J.Z. Zhu, *A simple error estimator and adaptive procedure for practical engineering analysis.* International Journal for Numerical Methods in Engineering, 1987. **24**: p. 337-357.
6. Zienkiewicz, O.C. and J.Z. Zhu, *The superconvergent patch recovery (SPR) and a-posteriori error estimates. Part 2: Error estimates and adaptivity.* International Journal for Numerical Methods in Engineering, 1992. **33**: p. 1365-1382.
7. Babuska, I. and A. Miller, *Post-processing approach in the finite element method. Part 3: a-posteriori error estimates and adaptive mesh selection.* International Journal for Numerical Methods in Engineering, 1984. **20**(12): p. 2311-2324.
8. Oden, J.T., W. Wu, and M. Ainsworth, *An a-posteriori error estimate for finite element approximations of the Navier-Stokes equations.* Computational Methods in Applied Mechanics and Engineering, 1993. **111**: p. 185-202.
9. Chang, S. and D.C. Haworth, *Adaptive grid refinement using cell-level and global imbalances.* International Journal for Numerical Methods in Fluids, 1997. **24**: p. 375-392.
10. Oden, J.T. and S. Prudhomme, *New approaches to error estimation and adaptivity for the Stokes and Oseen equations.* International Journal for Numerical Methods in Fluids, 1999. **31**: p. 3-15.
11. Oñate, E., et al., *Error estimation and mesh adaptivity in incompressible viscous flows using a residual power approach.* Computer Methods in Applied Mechanics and Engineering, 2006. **195**: p. 339-362.
12. Venditti, D.A. and D.L. Darmofal, *Adjoint error estimation and grid adaptation for functional outputs: application to quasi-one dimensional flow.* Journal of Computational Physics, 2000. **164**: p. 204-227.
13. Fidkowski, K.J. and D.L. Darmofal, *Review of output-based error estimation and mesh adaptation in computational fluid dynamics.* AIAA Journal, 2011. **49**(4): p. 673-694.
14. Dwight, R.P., *Heuristic a-posteriori estimation of error due to dissipation in finite volume schemes with application to mesh adaptation.* Journal of Computational Physics, 2008. **227**(5): p. 2845-2863.
15. Zhang, X.D., J.Y. Trépanier, and R. Camarero, *A posteriori error estimation for finite-volume solutions of hyperbolic conservation laws.* Computational Methods in Applied Mechanics and Engineering, 2000. **185**: p. 1-19.
16. Hay, A. and M. Visonneau, *Error estimation using the error transport equation for finite-volume methods and arbitrary meshes.* International Journal of Computational Fluid Dynamics, 2006. **20**(7): p. 463-479.
17. Shih, T. and Y. Qin, *A-posteriori method for estimating and correcting grid-induced errors in CFD solutions. Part 1: Theory and method.* AIAA Paper 2007-100, 2007.
18. Roy, C.J., *Strategies for driving mesh adaption in CFD.* AIAA Paper 2009-1302, 2009.

19. Muzaferija, S. and D. Gosman, *Finite-Volume CFD procedure and adaptive error control strategy for grids of arbitrary topology.* Journal of Computational Physics, 1996. **138**: p. 766-787.
20. Blottner, F.G. and A.R. Lopez, *Determination of solution accuracy of numerical schemes as part of code and calculation verification.* SANDIA report SAND98-2222, 1998.
21. Berger, M.J. and A. Jameson, *Automatic adaptive grid refinement for the Euler equations.* Retrieved from http://hdl.handle.net/2060/19840009909, 1985.
22. Baker, T.J., *Mesh adaptation strategies for problems in fluid dynamics.* Finite Elements in Analysis and Design, 1997. **25**: p. 243-273.
23. Aftosmis, M.J. and M. Berger, *Multilevel error estimation and adaptive h-refinement for cartesian meshes with embedded boundaries.* AIAA Paper 2002-0863, 2002.
24. Fulton, S.R., *On the accuracy of multigrid truncation error estimates.* Electronic Transactions on Numerical Analysis, 2003. **15**: p. 29-37.
25. Gao, H. and Z.J. Wang, *A residual-based procedure for hp-adaptation on 2D hybrid meshes.* AIAA Paper 2011-492, 2011.
26. Richardson, L.F., *The approximate arithmetical solution by finite differences of physical problems involving differential equations, with an application to the stresses in a masonry dam.* Philosophical Transactions of the Royal Society of London. Series A 210 1910. **(459-470)**: p. 307–357.
27. Richardson, L.F. and J.A. Gaunt, *The deferred approach to the limit.* Philosophical Transactions of the Royal Society of London, Series A 226, 1927. **636-646**: p. 299–349.
28. Cadafalch, J., et al., *Verification of finite volume computations on steady-state fluid flow and heat transfer.* Journal of Fluids Engineering, 2002. **24**(11-21).
29. Roy, C.J. and F.G. Blottner, *Methodology for turbulence model validation: application to hypersonic flows.* Journal of Spacecraft Rockets, 2003. **40**(3): p. 313-325.
30. Roy, C.J., *Grid convergence error analysis for mixed-order numerical schemes.* AIAA Journal, 2003. **41**: p. 595-604.
31. Salas, M.D., *Some observations on grid convergence.* Computers and Fluids, 2006. **35**(688-692).
32. Roache, P.J., *Perspective: a method for uniform reporting of grid refinement studies.* Journal of Fluids Engineering, 1994. **116**: p. 405-413.
33. Barth, T.J., *A 3D upwind euler solver for unstructured meshes.* AiAA Paper 1991-1548, 1991.
34. Zhang, Z. and A. Naga, *A new finite element gradient recovery method: superconvergence property.* SIAM Journal of Scientific Computing, 2005. **26**(4): p. 1192-1213
35. Cueto-Felgueroso, L., et al., *Finite volume solvers and moving least-squares approximations for the compressible Navier-Stokes equations on unstructured grids.* Computer Methods in Applied Mechanics and Engineering, 2007. **196**(45-48): p. 4712-4736.
36. Duarte, C.A. and J.T. Oden, *An h-p adaptive method using clouds.* Computer Methods in Applied Mechanics and Engineering, 1996. **139**: p. 237-262.
37. Liu, W.K., et al., *Multiresolution reproducing kernel particle method for computational fluid dynamics.* International Journal for Numerical Methods in Fluids 1997. **24**(12): p. 1391-1415.

38. Gavete, L., J.L. Cuesta, and A. Ruiz, *A numerical comparison of two different approximations of the error in a meshless method.* European Journal of Mechanics & Solids, 2002. **21**: p. 1037-1054.
39. Lee, C.K. and C.E. Zhou, *On error estimation and adaptive refinement for element free Galerking method. Part I: stress recovery and a posteriori error estimation.* Computer and Structures, 2004. **82**: p. 413-428.
40. Rabczuk, T. and T. Belytschko, *Adaptivity for structured meshfree particle methods in 2D and 3D.* International Journal for Numerical Methods in Engineering, 2005. **63**: p. 1559-1582.
41. Li, Q. and K.-M. Lee, *An adaptive meshless method for magnetic field computation.* IEEE Transactions on Magnetics, 2006. **42**(8): p. 1996-2003.
42. Angulo, A., L. Pérez Pozo, and F. Perazzo, *A posteriori error estimator and an adaptive technique in meshless finite point method.* Engineering Analysis with Boundary Elements, 2009. **33**(11): p. 1322-1338.
43. You, Y., J.S. Chen, and H. Lu, *Filters, reproducing kernel, and adaptive meshfree method.* Computational Mechanics, 2003. **31**(3-4): p. 316-326.
44. Perazzo, F., R. Löhner, and L. Perez-Pozo, *Adaptive methodology for meshless finite point method.* Advances in Engineering Software, 2007. **39**: p. 156-166.
45. Afshar, M.H. and M. Lashckarbolok, *Collocated discrete least-squares (CDLS) meshless method: Error estimate and adaptive refinement.* International Journal for Numerical Methods in Fluids, 2008. **56**: p. 1909-1928.
46. Boroomand, B., M. Najjar, and E. Oñate, *The generalized finite point method.* Computational Mechanics, 2009. **44**(2): p. 173-190.
47. Rüter, M. and J.S. Chen. *A multi-space error estimation approach for meshfree methods*. in *Conference Applications of Mathematics 2015*. 2015. Prague.
48. Oñate, E., et al., *A stabilized Finite Point Method for analysis of fluid mechanics problems.* Computer Methods in Applied Mechanics and Engineering, 1996. **139**: p. 315-346.
49. Löhner, R., et al., *A Finite Point Method for compressible flow.* International Journal for Numerical Methods in Engineering, 2002. **53**: p. 1765-1779.
50. Ortega, E., E. Oñate, and S. Idelsohn, *A finite point method for adaptive three-dimensional compressible flow calculations.* International Journal for Numerical Methods in Fluids, 2009. **60**: p. 937-971.
51. Ortega, E., E. Oñate, and S. Idelsohn, *An improved finite point method for three-dimensional potential flows.* Computational Mechanics, 2007. **40**: p. 949-963.
52. Ortega, E., et al., *Comparative accuracy and performance assessment of the finite point method in compressible flow problems.* Computer and Fluids, 2014. **59**: p. 53-65.
53. Fischer, T., *A contribution to adaptive numerical solution of compressible flow problems*. 1996, Universitat Politècnica de Catalunya.
54. Chen, R. and Y. Chen, *Error estimates for the finite point method.* Applied Numerical Mathematics, 2008. **58**(6): p. 884-898.
55. Katz, A., *Meshless methods for computational fluid dynamics*. 2009, Standford University.
56. Ortega E., O.E., Idelsohn S., Flores R.,, *Comparative accuracy and performance assessment of the Finite Point Method in compressible flow problems.* Computer and Fluids, 2014. **89**: p. 53-65.
57. Roe, P.L., *Approximate Riemann solvers, parameter vectors and difference schemes.* Journal of Computational Physics, 1981. **43**: p. 357-372.

58. Turkel, E., *Improving the accuracy of central difference schemes.* ICASE Report 88-53, 1988.
59. Van Albada, G.D., B. Van Leer, and W.W.J. Roberts, *A comparative study of computational methods in cosmic gas dynamics.* Astronomy and Astrophysics, 1982. **108**: p. 76-84.
60. Jameson, A., *Artificial diffusion, upwind biasing, limiters and their effect on accuracy and multigrid convergence in transonic and hypersonic flows.* AIAA-93-3359, 1993.
61. Jameson, A. and T.J. Baker, *Improvements to the aircraft Euler method.* AIAA Paper 87-0452, 1987.
62. Van Leer, B., *Towards the ultimate conservative difference scheme. V, A second order sequel to Godunov's method.* Journal of Computational Physics, 1979. **32**: p. 101-136.
63. Berger, M. and M.J. Aftosmis, *Analysis of slope limiters on irregular grids.* AIAA Paper 2005-0490, 2005.
64. Harten, A., et al., *Uniformly high-order accurate essential non-oscillatory schemes III.* Journal of Computational Physics, 1987. **71**: p. 231-303.
65. Liu, X., S. Osher, and T.F. Chen, *Weighted essential non-oscillatory schemes.* Journal of Computational Physics, 1994. **115**: p. 200-212.
66. Qiu, J. and C. Shu, *Hermite WENO schemes and their application as limiters for the Runge-Kutta discontinuous Galerking method: one dimensional case.* Journal of Computational Physics, 2003. **193**: p. 115-135.
67. Serna, S. and A. Marquina, *Power ENO methods: a fifth-order accurate Weighted Power ENO method.* Journal of Computational Physics, 2004. **194**: p. 632-658.
68. Zienkiewicz, O.C. and R.L. Taylor, *The finite element method, Volume 1*. 2000: Butterworth-Heinemann.
69. Ortega E., et al., *A meshless finite point method for three-dimensional analysis of compressible flow problems involving moving boundaries and adaptivity.* International Journal for Numerical Methods in Fluids, 2013. **73**(4): p. 323-343.
70. Loving, D. and B. Estabrooks, *Transonic-wing investigation in the Langley 8-foot high-speed tunnel at high subsonic Mach numbers and at a Mach number of 1.2. Analysis of pressure distribution of wing-fuselage configuration having a wing of 45º sweepback, aspect ratio 4, taper ratio 0.6, and NACA 65A006 airfoil section.* National Advisory Committee for Aeronautics. Research Memorandum NACA RM L51F07, 1951.